Correlative operando microscopy of oxygen evolution electrocatalysts

https://doi.org/10.1038/s41586-021-03454-x

Received: 19 February 2020

Accepted: 15 March 2021

Published online: 5 May 2021

Check for updates

J. Tyler Mefford[1,2]✉, Andrew R. Akbashev[1,2], Minkyung Kang[3], Cameron L. Bentley[3], William E. Gent[1], Haitao D. Deng[1], Daan Hein Alsem[4], Young-Sang Yu[5], Norman J. Salmon[4], David A. Shapiro[5], Patrick R. Unwin[3] & William C. Chueh[1,2]✉

Transition metal (oxy)hydroxides are promising electrocatalysts for the oxygen evolution reaction[1–3]. The properties of these materials evolve dynamically and heterogeneously[4] with applied voltage through ion insertion redox reactions, converting materials that are inactive under open circuit conditions into active electrocatalysts during operation[5]. The catalytic state is thus inherently far from equilibrium, which complicates its direct observation. Here, using a suite of correlative operando scanning probe and X-ray microscopy techniques, we establish a link between the oxygen evolution activity and the local operational chemical, physical and electronic nanoscale structure of single-crystalline β-$Co(OH)_2$ platelet particles. At pre-catalytic voltages, the particles swell to form an α-$CoO_2H_{1.5}.0.5H_2O$-like structure—produced through hydroxide intercalation—in which the oxidation state of cobalt is +2.5. Upon increasing the voltage to drive oxygen evolution, interlayer water and protons de-intercalate to form contracted β-CoOOH particles that contain Co^{3+} species. Although these transformations manifest heterogeneously through the bulk of the particles, the electrochemical current is primarily restricted to their edge facets. The observed Tafel behaviour is correlated with the local concentration of Co^{3+} at these reactive edge sites, demonstrating the link between bulk ion-insertion and surface catalytic activity.

The oxygen evolution reaction (OER; $4OH^- \rightarrow O_2 + 2H_2O + 4e^-$) is the anodic half-reaction in the electrolytic generation of hydrogen from water, and has a standard electrode potential (E^0) of 0.401 V versus the standard hydrogen electrode (SHE) and a formal potential ($E^{0'}$) of 1.229 V versus the reversible hydrogen electrode (RHE). This reaction is acknowledged as the efficiency bottleneck of the process, as it requires considerable applied overpotential[3] ($\eta_{OER} = E - E_{O_2/OH^-} > 0.3$ V). Improving the efficiency of the OER is therefore crucial to realize a closed-loop clean energy infrastructure based on the generation and storage of hydrogen gas. This will require the development of improved transition-metal-based electrocatalysts by directly identifying how evolving material properties influence reactivity during operation.

Only the surface catalyses the OER

Our work uses single-crystalline β-$Co(OH)_2$ platelet particles (Fig. 1a) with basal plane {0001} facets of approximately 1–2 μm wide and edge {10$\bar{1}$0} facets of around 50–75 nm thick. The scanning electron microscopy (SEM) images[5,6] of these particles are shown in Fig. 1b, c. These particles exhibit two bulk redox transformations with increasing anodic voltage at $E_1^{0'} \approx 1.20$ V and $E_2^{0'} \approx 1.55$ V versus RHE, which have previously been assigned to the conversion of $Co(OH)_2$ to CoOOH and of CoOOH to CoO_2, respectively[5]. The OER was observed to begin concomitantly with the second bulk redox process at $E > 1.55$ V versus RHE (Fig. 1d). The voltages of these reactions have previously been observed to scale linearly with pH (−59 mV/pH versus SHE) and we use the formal potential, $E^{0'}$, to describe the reversible voltage on the pH-independent RHE scale[6]. Note that all voltages in this work are referenced against the RHE unless stated otherwise.

To investigate the dependence of the rate of the OER on the active-site concentration, the OER current (j_{OER}; Fig. 1e) and pre-catalytic redox capacity (Q_a, Fig. 1f) were first investigated as a function of scan rate at sub-monolayer mass loadings on glassy carbon rotating disk electrodes (RDE). To ensure that residual material transformations did not obscure the relationship between the extent of Co oxidation and OER activity, we cycled the electrodes between 1.0 V and 1.75 V, starting at 1,000 mV s^{-1} and moving to progressively slower scan rates in each successive cycle. At 1,000 mV s^{-1}, each Co atom in the electrode is oxidized on average by $Q_a \approx 0.02e^-$ in the pre-catalytic region, and this increases to around $0.5e^-$ per Co atom when the scan rate is decreased by four orders of magnitude to 0.25 mV s^{-1}. Thus, this regime of reactivity corresponds to transformations that extend throughout the bulk of the particles. Notably, the total amount of charge passed at a given scan rate scales linearly with mass loading, which confirms the absence of limitations in active mass utilization at these electrode loadings[6].

[1]Department of Materials Science and Engineering, Stanford University, Stanford, CA, USA. [2]Stanford Institute for Materials and Energy Sciences, SLAC National Accelerator Laboratory, Menlo Park, CA, USA. [3]Department of Chemistry, University of Warwick, Coventry, UK. [4]Hummingbird Scientific, Lacey, WA, USA. [5]Advanced Light Source, Lawrence Berkeley National Laboratory, Berkeley, CA, USA. ✉e-mail: tmefford@stanford.edu; wchueh@stanford.edu

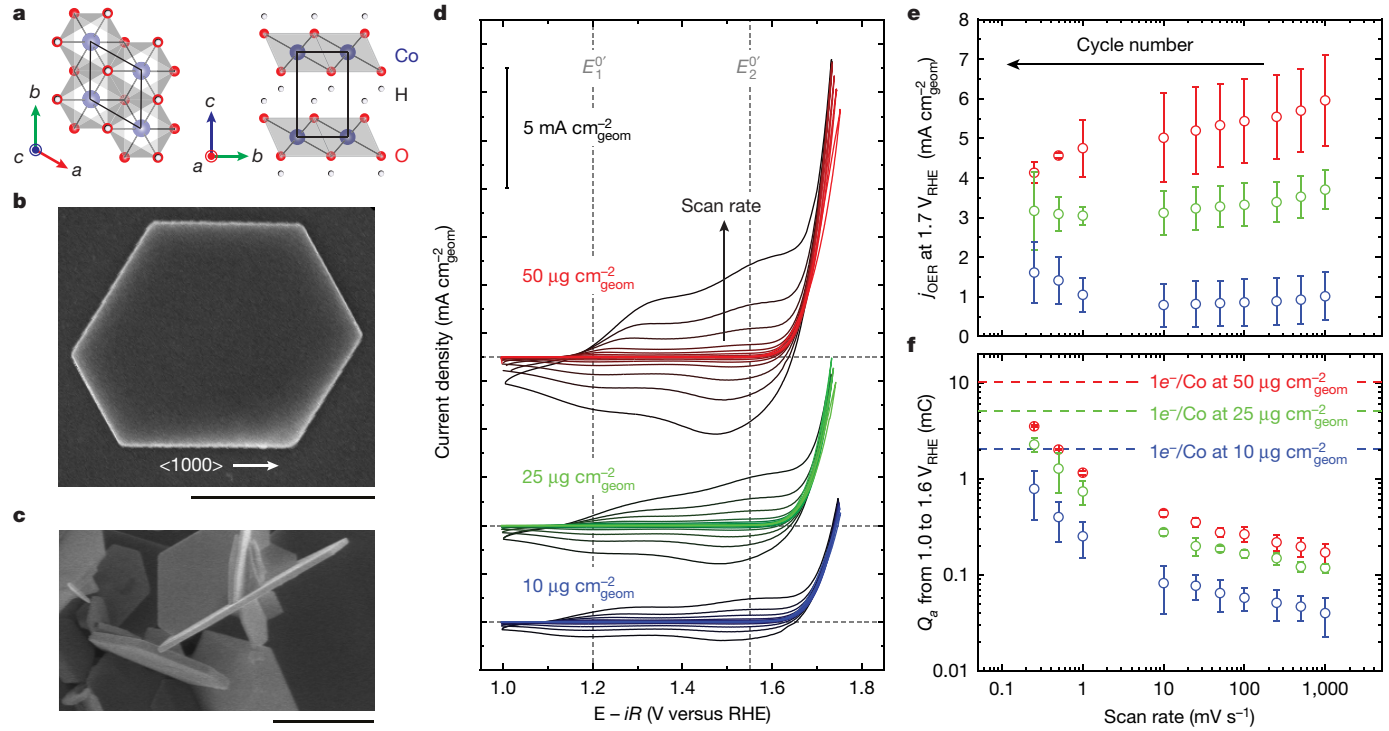

Fig. 1 | Mass loading and scan-rate-dependent electrochemistry of β-Co(OH)$_2$. a, Crystal structure of β-Co(OH)$_2$ along the [001] and [100] axes. **b**, **c**, SEM images of the {0001} basal plane (**b**) and {10$\bar{1}$0} edge facets (**c**) of the particles. Scale bars, 1 µm. **d**, RDE cyclic voltammograms at mass loadings of 10, 25 and 50 µg cm$^{-2}_{geom}$ (corresponding to electrode coverages[6] of around 0.2, 0.5 and 0.8, respectively), scan rates between 0.25–1,000 mV s^{-1} and a rotation rate of 1,600 rpm in O_2-saturated 0.1 M KOH. **e**, **f**, OER current density, j_{OER}, at 1.7 V (**e**) and anodic bulk redox charge, Q_a, evaluated from 1.0–1.6 V as a function of scan rate and mass loading (**f**). Colours correspond to the labels in **d**. Error bars represent s.d. of triplicate measurements.

In contrast to the extent of bulk Co oxidation, the OER current is not dependent on the scan rate. We found that j_{OER} at 1.7 V is not statistically different at 0.25 mV s^{-1} than at 1,000 mV s^{-1}, but it does scale approximately linearly with mass loading, as previously described[6]. The OER is therefore already at steady state at 1,000 mV s^{-1}. These results preclude catalysis occurring in the interior of the particles, in contrast to previous hypotheses for metal hydroxide electrocatalysts[7]. We note that no change in OER activity was observed in the presence of iron impurities in the electrolyte, suggesting that our model single crystal particles have a low concentration of defects[8].

The edge facets are the active surfaces

We directly mapped the OER current using scanning electrochemical cell microscopy (SECCM), at a spatial resolution determined by the diameter of the nanopipette tip (d_{tip} = 440 nm) (Fig. 2a). A detailed description of the technique can be found in recent reviews on the topic[9–11].

We used two modes of SECCM, which offer complementary information on the connection between local OER activity and bulk oxidation. First, in scanning mode, chronoamperometry was performed at 1.87 V while the pipette was raster-scanned linearly and continuously across the particles (lateral translation rate = 30 nm s^{-1}). This provides simultaneous topography (height) and electrochemical activity (current) measurements by maintaining a constant contact between the meniscus and the surface. The results (Fig. 2c, d) demonstrate that the particle edge facets dominate the electrochemical reactivity of the system. For the particles shown in Fig. 2d, current is observed only when the pipette encompasses the edge of the particles (bottom), not when it is on top of the basal plane (top).

In hopping-mode SECCM (Fig. 2b, e, f, Supplementary Video 1), the pipette was raster-scanned stepwise across the particles (that is, electrolyte contact with the surface is broken and re-established during each step) and linear sweep voltammetry was performed at a scan rate of 1,000 mV s^{-1} at each step. Simultaneous topographical (Fig. 2f, top) and voltammetric (Fig. 2f, bottom) mapping of the electrochemical response across the particles again revealed that the particle edge facets have high electrochemical activity compared with the low activity of the basal planes. The latter show currents similar to those of the baseline glassy carbon support (Fig. 2b). Variations in current at the edges of the two isolated particles on the right-hand side of the images in Fig. 2f correlate with particle thickness—thinner particles generate lower currents at a given voltage. Some of the observed variation in edge activity might also arise from defects at the edge facets[11], as demonstrated by the scan across the edge of a particle fragment (Fig. 2d). These results directly confirm previous hypotheses that the basal planes of the CoO_xH_y system are inactive[5,6,12].

The active site for the OER is expected to be[5] an oxidized phase of CoO_xH_y in which $y/x \leq 0.5$ (generally $x = 2$). The different activity of these facets can therefore be rationalized by the ion (de)intercalation characteristics of the system, in which mobile charge-compensating ions are restricted to the interlayer gallery between the CoO_2 slabs. In the progressive oxidation of layered β-Co(OH)$_2$, ion (de)intercalation is facilitated at the edge facets—at the regions that are in contact with the electrolyte. By contrast, ion movement in the <0001> direction is restricted in the absence of extended defects in the CoO_2 layers, which prevents the basal planes from serving as reaction sites to initiate the bulk redox transformation reactions. This also explains the lack of activity of interior Co atoms. We also note that oxidized CoO_xH_y compositions exhibit higher electronic conductivity[13], which may influence the observed current density at the basal planes, for which the absence of ion (de)intercalation prevents the formation of more conductive CoO_xH_y compositions.

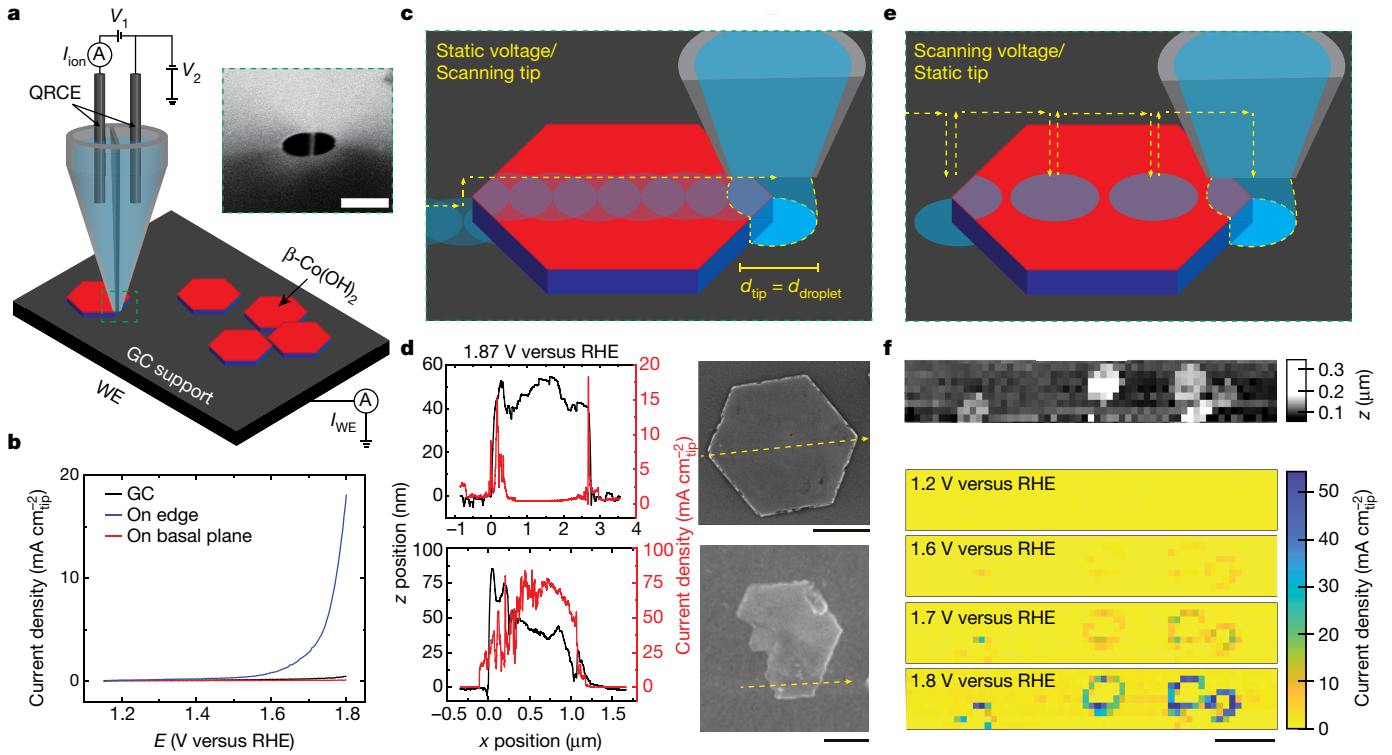

Fig. 2 | SECCM of bulk redox transformations and OER activity of β-Co(OH)$_2$ particles. a, Schematic demonstrating the SECCM technique. A laser-pulled dual-barrel pipette with tip diameter (d_{tip} = 440 nm, shown in the field emission (FE)-SEM image in the inset; scale bar, 400 nm) corresponding to the interrogation spot size, contains the electrolyte (0.1 M KOH) and a quasi-reference counter electrode (QRCE; AgCl-coated Ag wire) within each barrel. A glassy carbon (GC) support with dispersed isolated β-Co(OH)$_2$ particles serves as the working electrode (WE) where the voltage, V_2, and current, I_{WE}, can be controlled and measured. The pipette height is controlled by monitoring the ion current, I_{ion}, between the two barrels when a voltage signal, V_1, is applied between the two QRCEs. **b**, Comparison of electrochemical reactivity for the glassy carbon support and for the edge facet and basal plane facets of the β-Co(OH)$_2$ particles at a scan rate of 1 V s^{-1}. **c**, Scanning-mode SECCM using a constant voltage (1.87 V) and constant lateral scanning rate (30 nm s^{-1}). **d**, Tip current density as a function of position in scanning constant height mode for the particles shown in the FE-SEM images on the right. The scan direction is indicated by the dotted yellow arrows and the interrogation width is approximately 400 nm. Scale bars, 1 μm. **e**, Hopping-mode SECCM, in which a linear sweep voltammogram (scan rate = 1 V s^{-1}) is obtained at each point. **f**, Topography and local current density maps at increasing applied voltage. Scale bar, 5 μm. There is no interpolation of the pixel-level data in **f**.

Hydroxide ions are (de)intercalated

Changes in particle morphology with voltage were measured at a spatial resolution of around 10 nm in 0.1 M KOH using electrochemical atomic force microscopy[14–17] (EC-AFM) (Fig. 3, Supplementary Video 2). The cell design is shown in Supplementary Fig. 1. The EC-AFM results are complemented by correlative isothermal (at a temperature, T, of 25 °C) electrochemical quartz crystal microbalance (EQCM) mass measurements (Fig. 3c; a comparison to a blank Pt EQCM electrode is included in Supplementary Fig. 2). Scan rates of 5 mV min^{-1} were used for both EQCM and EC-AFM to approach the steady state behaviour of the system.

During oxidation, the particle morphology evolves non-monotonically with voltage, shown in both single point (Fig. 3b, c) and line scan (Fig. 3a, d) profiles. At $E_1^{0'} \approx 1.2$ V, the particle height expands by approximately 10% on average (Fig. 3c), in contrast to the volume contraction that would be expected[5] for the formation of CoOOH but similar to previously reported EC-AFM data obtained for single-layer CoO_xH_y after cycling[14]. This change in height is correlated with a measured lateral expansion of the particle (Fig. 3d), reaching a maximum at an intermediate voltage of 1.39 V. Around $E_2^{0'} \approx 1.58$ V, the particle contracts back to almost its initial dimensions.

Differential height images (normalized by the initial particle height at 0.96 V) (Fig. 3b) and line scans (Fig. 3d, bottom) emphasize the local heterogeneity in the evolving morphology. Starting at E = 1.12 V, expanded regions of the particle nucleate heterogeneously and spread radially towards the interior and edges with increasing voltage. At values of E between 1.3 V and 1.5 V, the particle has an expanded hexagonal interior region (where the edges of the hexagon are aligned with the original edge facets of the particle) surrounded by a hexagonal ring of around 100 nm thick and of unchanged height, and then a region of apparent marked height increase (which manifests as a yellow to red hexagonal ring at the outer edge of the particle). The large height differences at these outer regions correspond to particle expansion outwards past the edges of the original open-circuit state. Figure 3d shows increased lateral expansion at the base of the particles (closest to the substrate), suggesting a preferred direction of translation for the individual CoO_xH_y layers. Finally, as the voltage increases further the particle contracts, starting from the outer edges and moving inwards towards the centre of the particle.

From EQCM measurements, we found a mass-to-charge ratio of m/z = 16.7 ± 0.8 g per mole e^- for the first redox transition (from 0.9 to 1.36 V), which suggests hydroxide intercalation (m/z = 17.01 g per mole e^-) rather than proton de-intercalation as the coupled ion-insertion reaction. An observed mass change corresponding to 0.56 ± 0.2 moles of OH^- inserted per mole of Co suggests an intermediate phase of $CoO_2H_{1.5}{\cdot}0.5H_2O$ according to the reaction shown below; we assign this as the α phase owing to the presumed formation of interlayer water, as seen for other hydroxide systems such as α-Ni(OH)$_2$ and Co-layered double hydroxide:[18,19]

$$\beta - Co(OH)_2 + 0.5OH^- \rightleftharpoons \alpha - CoO_2H_{1.5} \cdot 0.5H_2O + 0.5e^-$$

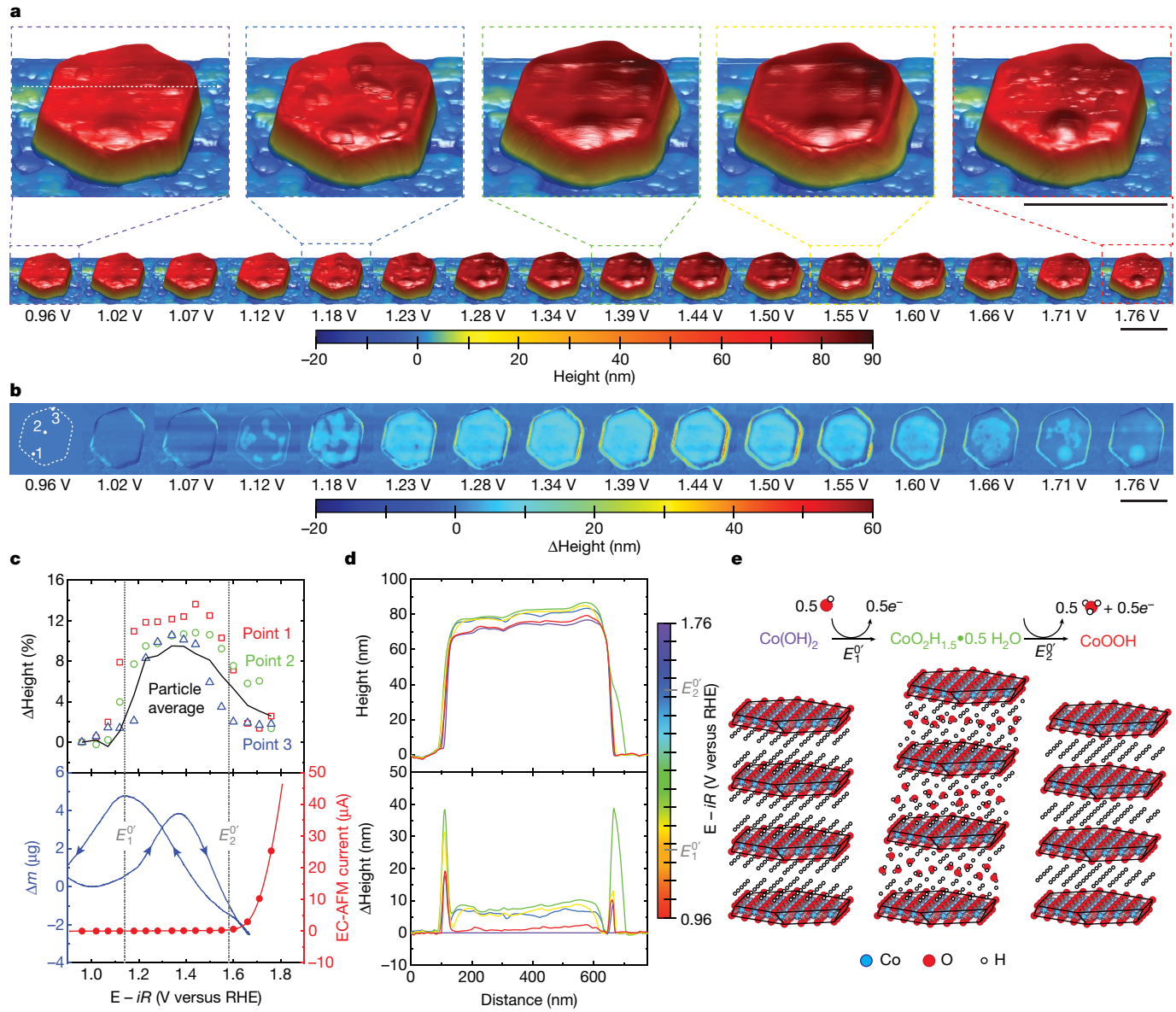

Fig. 3 | Operando EC-AFM of a β-Co(OH)$_2$ particle. a, Topography of a β-Co(OH)$_2$ particle in 0.1 M KOH at different applied voltages. Scale bars, 500 nm. **b**, Differential height compared to the particle morphology at the open-circuit voltage (0.96 V). Scale bar, 500 nm. **c**, Top, Heights measured at three selected points (shown on the particle at 0.96 V in **b**); bottom, EC-AFM current (linear sweep voltammetry, red line) and isothermal (T = 25 °C) mass change (measured by EQCM) with changing voltage (blue line). Both EC-AFM and EQCM experiments were performed at a scan rate of 5 mV min^{-1}. The EQCM used a mass loading of 100 μg cm$^{-2}_{geom}$ β-Co(OH)$_2$ on a Pt-coated quartz crystal. **d**, Line scan of particle height (top) and change in particle height (bottom) versus voltage for the line drawn on the magnified views of the particle at 0.96 V in **a**. **e**, Schematic demonstrating the translation and the expansion and contraction of individual CoO_2 layers as the voltage is increased.

Because the particles are oxidized during the second reaction at $E_2^{0'}$, EQCM measurements reveal a decrease in mass; this suggests that interlayer water and additional protons are removed as the particle contracts to form β-CoOOH (observed in post-mortem X-ray diffraction experiments; see Supplementary Information). However, interpretation of mass changes in this voltage region is complicated by the formation of gas bubbles at the electrode surface due to the OER, which results in a lower local viscosity at the electrode–electrolyte interface, thus increasing the resonant frequency and obscuring the total mass change[20].

The insertion and removal of OH^- ions, as evidenced through the EQCM measurements, explain the observed volume changes observed by EC-AFM. A schematic summarizing the structural changes is shown in Fig. 3e. Upon oxidation, OH^- intercalates into β-Co(OH)$_2$ to form the expanded α-$CoO_2H_{1.5}$·0.5H_2O structure. CoO_2 layers can translate considerably during this process owing to the reduction in van der Waals and hydrogen-bonding forces as a result of the interlayer water. The layer translations show some preferential directionality (Supplementary Video 2). This effect is well documented in hydroxide systems, in which the simultaneous presence of α- and β-phases results in turbostratic disordering during oxidation and particle expansion[21–24]. As the voltage increases, the increasing oxidation state of Co results in a decrease in the Co–O bond length, causing layer translation and particle contraction to a stabilized β-CoOOH structure that lacks the interlayer water that is present in the intermediate state.

Voltage-dependent Co oxidation states

We investigated the local Co oxidation state across the particles at a spatial resolution of 50 nm using operando scanning transmission

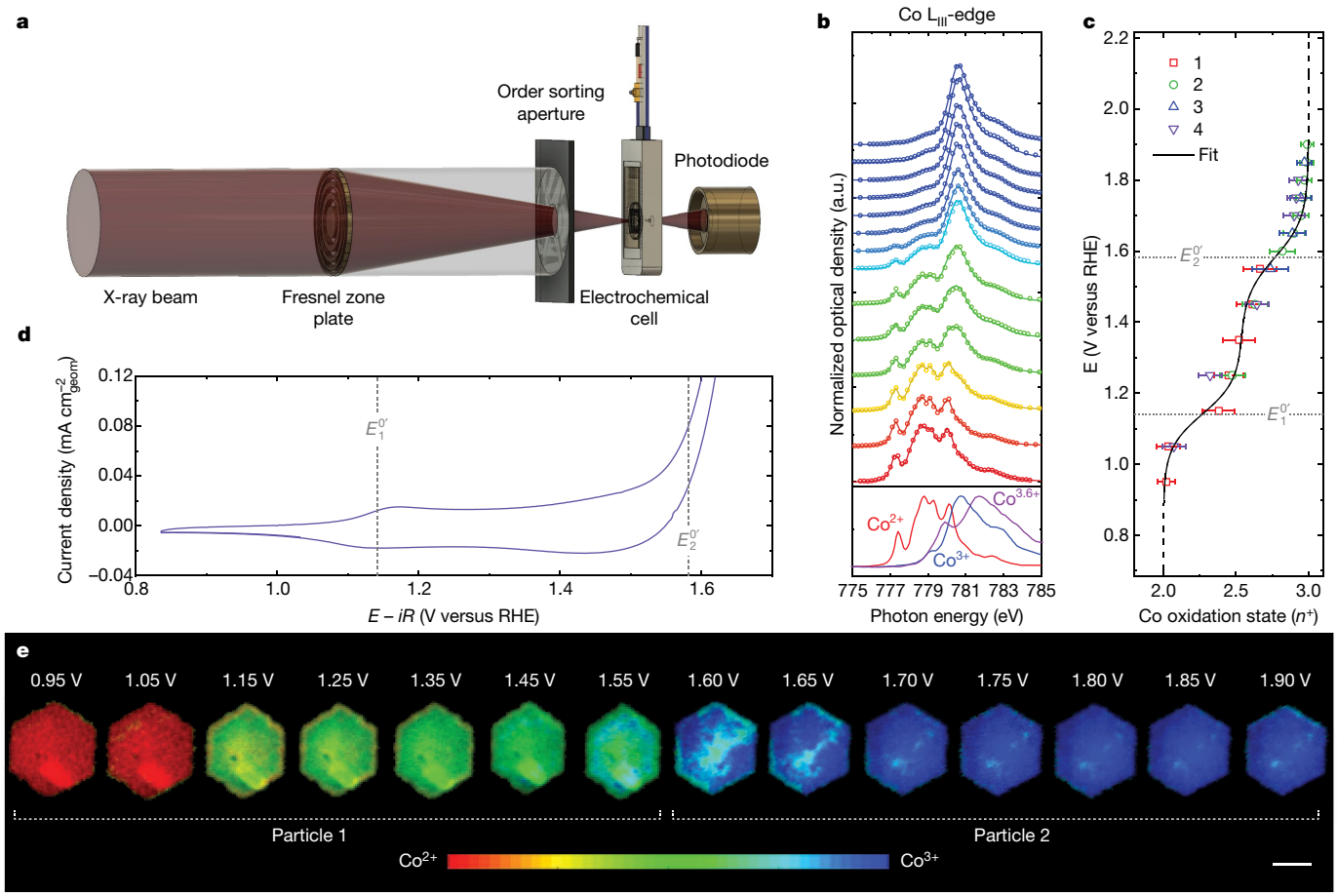

Fig. 4 | Operando STXM of β-Co(OH)$_2$ particles. a, Experimental setup showing the electrochemical flow cell coupled into the STXM microscope. **b**, Voltage-dependent particle-averaged Co L$_{III}$-edge STXM-XAS spectra. Spectra are offset with their optical density intercept at 775 eV corresponding to the steady-state voltage at which the data was acquired. The spectra represent the average of all single-pixel STXM–XAS spectra for a single particle. Reference spectra are included for the as synthesized β-Co(OH)$_2$ (Co^{2+}), LiCoO$_2$ (Co^{3+}) and Sr$_6$Co$_5$O$_{15}$ (Co$^{3.6+}$). **c**, Co oxidation state plotted with voltage, with an ideal solution model fit for four separate particles. Error bars represent the s.d. of the single-pixel STXM–XAS spectra across the particle. **d**, Cyclic voltammogram (in 0.1 M KOH) of β-Co(OH)$_2$ in the STXM electrochemical flow cell at a scan rate of 10 mV s^{-1} and a flow rate of 30 µl min^{-1}. **e**, Steady-state voltage-dependent Co oxidation state phase maps of β-Co(OH)$_2$ particles 1 and 2. Scale bar, 1 µm.

X-ray microscopy (STXM) at the Co L$_{III}$-edge[25]. The experimental setup is shown in Fig. 4a and Supplementary Fig. 3.

Averaging the single-pixel STXM–X-ray absorbance spectroscopy (XAS) measurements across a single particle yields the particle-averaged X-ray absorbance spectrum (Fig. 4b). Figure 4c shows the corresponding Co oxidation state plotted with voltage; the oxidation states are derived from a linear combination fit of the particle-averaged X-ray absorbance spectrum to end members derived from non-negative matrix factorization. The distribution in measured oxidation states was investigated using four separate particles (Supplementary Fig. 4). We fit a Nernstian ideal solution model to the data to approximate the solid-state redox reactions of the β-Co(OH)$_2$ particles (Supplementary Figs. 5–8). The model extracts both the number of electrons transferred per redox reaction and the corresponding reversible voltages from XAS, $n_1 = 0.54 \pm 0.04\ e^-$ at $E_1^{0'} = 1.14 \pm 0.03$ V and $n_2 = 0.46 \pm 0.04\ e^-$ at $E_2^{0'} = 1.58 \pm 0.03$ V. The derived reversible voltages show excellent agreement with the redox peaks in the STXM cell (Fig. 4d), RDE experiments (Fig. 1d), EC-AFM and EQCM results[6] (Fig. 3c); in addition, the number of electrons transferred during each reaction corresponds well with our EQCM results.

Notably, despite the nanoscale spatial resolution of STXM compared to bulk Co K-edge X-ray absorption near edge structure experiments, no regions of Co^{4+} (nor principal component analysis or non-negative matrix factorization components contributing more than 1% to the data variance; Supplementary Fig. 4) are observed, in contrast with previous reports on the Co–H$_2$O system[26–29]. Although the lack of extended structure and the high defect concentration in amorphous systems could enable the generation[28,29] of Co^{4+}, ultraviolet–visible absorption (UV–Vis) spectroelectrochemical experiments on our β-Co(OH)$_2$ system (Supplementary Fig. 9) yield nearly identical results to those reported for the amorphous 'CoCat' system (a full discussion on UV–vis spectroscopy results and the assignments of Co^{4+} in previous work is included in the Supplementary Information)[28]. Our observations therefore alter the assignments of the observed redox peaks for the CoO$_x$H$_y$ system, with $E_1^{0'}$ resulting in an average oxidation state of Co$^{2.54+}$, rather than Co^{3+}, and $E_2^{0'}$ resulting in an average oxidation state of Co^{3+}, rather than Co^{4+}.

Having elucidated the evolution of the average oxidation state of CoO$_x$H$_y$, we plotted nanoscale phase maps (Fig. 4e) that show the local Co oxidation state with 50 nm spatial resolution. During the oxidation processes at both $E_1^{0'}$ and $E_2^{0'}$, considerable heterogeneity develops at the subparticle level, with preferential oxidation of the interior of the platelets while the edge regions maintain lower oxidation states. This observation is consistent with the morphological heterogeneity observed in the EC-AFM experiments and could reflect chemomechanical effects caused by a turbostratic intergrowth of α-CoO$_2$H$_{1.5}$·0.5H$_2$O (with interlayer water) and β-Co(OH)$_2$ or β-CoOOH[23]. We note that the reduced edge features are unlikely to be a result of

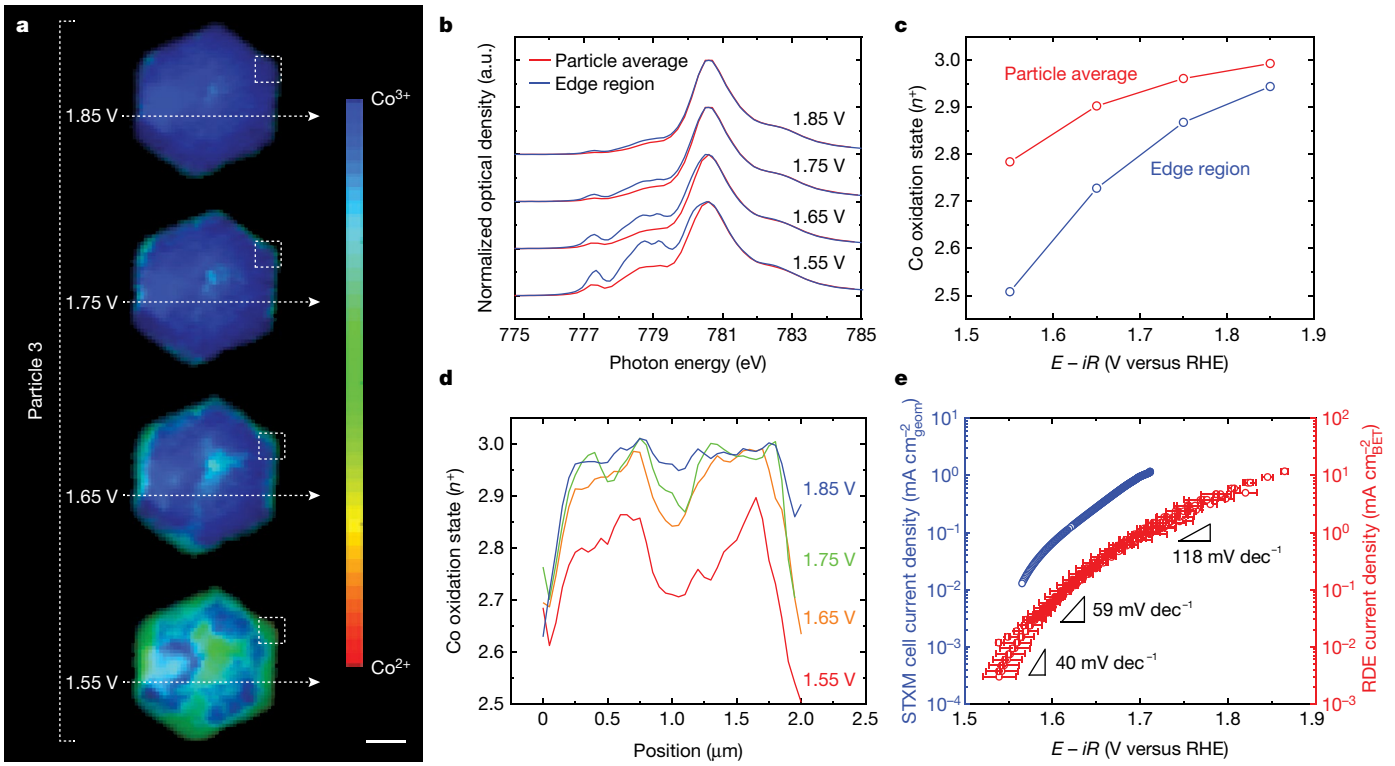

Fig. 5 | Correlations between Co oxidation state at the edge of the particles and OER activity. a, Phase maps of a β-$Co(OH)_2$ particle at applied voltages in different OER Tafel regions. Scale bar, 500 nm. **b**, Co L_{III}-edge STXM–XAS spectra of the particle average and the boxed edge region in **a**, showing a reduced Co oxidation state at the edge of the particles. **c**, Corresponding Co oxidation state for the full particle average and edge region from the Co L_{III}-edge XAS spectra in **b**. **d**, Co oxidation state line scans for the lines shown in **a**. **e**, OER Tafel data taken in the STXM cell and in a macroscopic RDE cell at a scan rate of 10 mV s^{-1}.

photoreduction from radiolysis effects, owing to the high exchange rate of electrolyte in the cell (Supplementary Information, Supplementary Figs. 10, 11).

Oxygen evolution is catalysed by Co^{3+}

We found that the observed Tafel slope is directly correlated to the local Co oxidation state (Co^{3+} coverage) at the reactive edge sites (Fig. 5). The voltage-dependent phase maps, edge region X-ray absorption spectrum and line scans all confirm that an increase in the Co oxidation state at the edges is associated with an increase in the Tafel slope from 40 mV dec^{-1} to 120 mV dec^{-1} (Fig. 5e). In addition, the reversible voltage for the conversion to CoOOH of $E_2^{0'}$ = 1.58 V corresponds reasonably well with our previous microkinetic modelling prediction[5] of $E^0_{\text{phasechange}}$ = 1.593 V. On the basis of the observed operando STXM data and our microkinetic modelling work[5], the low coverage of CoOOH at the edge (oxidation state +2.5) at 1.55 V corresponds to the high-activity Tafel slope of 40 mV dec^{-1}. As the voltage increases, so does the coverage of CoOOH, approaching saturation (Co oxidation state around +3) at E > 1.75 V and a Tafel slope of 120 mV dec^{-1}. These operando STXM results confirm that Co^{3+} (β-CoOOH) is the active site (or reactant state of the rate-limiting step) for the OER[30]. We note that the chemical reduction of the edges of the particles by ambient water is also observed after relaxation, as shown in Supplementary Fig. 12 and discussed in the Supplementary Information.

Conclusions and outlook

In this work, correlative operando microscopy is used to reveal how the local operational chemical, physical and electronic structure of an energy-conversion material governs its electrochemical response. In the CoO_xH_y system, hydroxide ion (de)intercalation reactions influence surface catalytic activity by controlling the relationship between OER overpotential and voltage-dependent Co^{3+} active-site concentration at the reactive edge facets. These results suggest that the OER activity of layered oxides can be improved using strategies that tune the thermodynamics of bulk ion insertion as well as by surface adsorption energy approaches.

Online content

Any methods, additional references, Nature Research reporting summaries, source data, extended data, supplementary information, acknowledgements, peer review information; details of author contributions and competing interests; and statements of data and code availability are available at https://doi.org/10.1038/s41586-021-03454-x.

1. Burke, M. S., Enman, L. J., Batchellor, A. S., Zou, S. & Boettcher, S. W. Oxygen evolution reaction electrocatalysis on transition metal oxides and (oxy)hydroxides: activity trends and design principles. *Chem. Mater.* **27**, 7549–7558 (2015).
2. Hong, W. T. et al. Toward the rational design of non-precious transition metal oxides for oxygen electrocatalysis. *Energy Environ. Sci.* **8**, 1404–1427 (2015).
3. Dau, H. et al. The mechanism of water oxidation: from electrolysis via homogeneous to biological catalysis. *ChemCatChem* **2**, 724–761 (2010).
4. Kuai, C. et al. Phase segregation reversibility in mixed-metal hydroxide water oxidation catalysts. *Nat. Catal.* **3**, 743–753 (2020).
5. Mefford, J. T., Zhao, Z., Bajdich, M. & Chueh, W. C. Interpreting Tafel behavior of consecutive electrochemical reactions through combined thermodynamic and steady state microkinetic approaches. *Energy Environ. Sci.* **13**, 622–634 (2020).
6. Mefford, J. T., Akbashev, A. R., Zhang, L. & Chueh, W. C. Electrochemical reactivity of faceted β-$Co(OH)_2$ single crystal platelet particles in alkaline electrolytes. *J. Phys. Chem. C* **123**, 18783–18794 (2019).
7. Doyle, A. D., Bajdich, M. & Vojvodic, A. Theoretical insights to bulk activity towards oxygen evolution in oxyhydroxides. *Catal. Lett.* **147**, 1533–1539 (2017).
8. Burke, M. S., Kast, M. G., Trotochaud, L., Smith, A. M. & Boettcher, S. W. Cobalt–iron (oxy) hydroxide oxygen evolution electrocatalysts: the role of structure and composition on activity, stability, and mechanism. *J. Am. Chem. Soc.* **137**, 3638–3648 (2015).

9. Wahab, O. J., Kang, M. & Unwin, P. R. Scanning electrochemical cell microscopy: A natural technique for single entity electrochemistry. *Curr. Opin. Electrochem.* **22**, 120–128 (2020).
10. Bentley, C. L. et al. Nanoscale electrochemical mapping. *Anal. Chem.* **91**, 84–108 (2019).
11. Bentley, C. L., Kang, M. & Unwin, P. R. Nanoscale structure dynamics within electrocatalytic materials. *J. Am. Chem. Soc.* **139**, 16813–16821 (2017).
12. Bajdich, M., García-Mota, M., Vojvodic, A., Nørskov, J. K. & Bell, A. T. Theoretical investigation of the activity of cobalt oxides for the electrochemical oxidation of water. *J. Am. Chem. Soc.* **135**, 13521–13530 (2013).
13. Stevens, M. B. et al. Ternary Ni-Co-Fe oxyhydroxide oxygen evolution catalysts: Intrinsic activity trends, electrical conductivity, and electronic band structure. *Nano Res.* **12**, 2288–2295 (2019).
14. Dette, C., Hurst, M. R., Deng, J., Nellist, M. R. & Boettcher, S. W. Structural evolution of metal (oxy)hydroxide nanosheets during the oxygen evolution reaction. *ACS Appl. Mater. Interfaces* **11**, 5590–5594 (2019).
15. Toma, F. M. et al. Mechanistic insights into chemical and photochemical transformations of bismuth vanadate photoanodes. *Nat. Commun.* **7**, 12012 (2016).
16. Kamachi, M. U. & Padhy, N. Electrochemical scanning probe microscope (EC-SPM) for the in situ corrosion study of materials: an overview with examples. *Corros. Rev.* **29**, 73–103 (2011).
17. Deng, J. et al. Morphology dynamics of single-layered $Ni(OH)_2$/NiOOH nanosheets and subsequent Fe incorporation studied by in situ electrochemical atomic force microscopy. *Nano Lett.* **17**, 6922–6926 (2017).
18. Bernard, P. et al. AC quartz crystal microbalance applied to the studies of the nickel hydroxide behaviour in alkaline solutions. *Electrochim. Acta* **36**, 743–746 (1991).
19. Young, M. J., Kiryutina, T., Bedford, N. M., Woehl, T. J. & Segre, C. U. Discovery of anion insertion electrochemistry in layered hydroxide nanomaterials. *Sci. Rep.* **9**, 2462 (2019).
20. Li, F., Hillman, A. R., Lubetkin, S. D. & Roberts, D. J. Electrochemical quartz crystal microbalance studies of potentiodynamic electrolysis of aqueous chloride solution: surface processes and evolution of H_2 and Cl_2 gas bubbles. *J. Electroanal. Chem. (Lausanne)* **335**, 345–362 (1992).
21. Cherepanova, S., Leont'eva, N., Drozdov, V. & Doronin, V. Thermal evolution of Mg-Al and Ni-Al layered double hydroxides: the structure of the dehydrated phase. *Acta Crystallogr. A* **72**, 651–659 (2016).
22. Ma, R. et al. Tetrahedral Co(II) coordination in α-type cobalt hydroxide: Rietveld refinement and X-ray absorption spectroscopy. *Inorg. Chem.* **45**, 3964–3969 (2006).
23. Hall, D. S., Lockwood, D. J., Bock, C. & MacDougall, B. R. Nickel hydroxides and related materials: a review of their structures, synthesis and properties. *Proc. R. Soc. A* **471**, 20140792 (2015).
24. Liu, S., Li, L., Patterson, N. A. & Manthiram, A. Morphological transformations during in situ electrochemical generation of 2-dimensional Co_3O_4 hexagonal nanoplates. *J. Electrochem. Soc.* **163**, A150–A155 (2016).
25. Lim, J. et al. Origin and hysteresis of lithium compositional spatiodynamics within battery primary particles. *Science* **353**, 566–571 (2016).
26. Gerken, J. B. et al. Electrochemical water oxidation with cobalt-based electrocatalysts from pH 0–14: the thermodynamic basis for catalyst structure, stability, and activity. *J. Am. Chem. Soc.* **133**, 14431–14442 (2011).
27. McAlpin, J. G. et al. EPR evidence for Co(IV) species produced during water oxidation at neutral pH. *J. Am. Chem. Soc.* **132**, 6882–6883 (2010).
28. Risch, M. et al. Water oxidation by amorphous cobalt-based oxides: in situ tracking of redox transitions and mode of catalysis. *Energy Environ. Sci.* **8**, 661–674 (2015).
29. Kanan, M. W. et al. Structure and valency of a cobalt-phosphate water oxidation catalyst determined by in situ X-ray spectroscopy. *J. Am. Chem. Soc.* **132**, 13692–13701 (2010).
30. Bergmann, A. et al. Unified structural motifs of the catalytically active state of Co(oxyhydr)oxides during the electrochemical oxygen evolution reaction. *Nat. Catal.* **1**, 711–719 (2018).

Data availability

The experimental data that support the findings of this study are available in ref. [31].

31. Mefford, J. T. Replication data for "Correlative operando microscopy of oxygen evolution electrocatalysts". https://doi.org/10.7910/DVN/TNTHXS (2021).

Acknowledgements J.T.M., A.R.A., W.E.G. and W.C.C. acknowledge funding provided by the US Department of Energy (DOE), Office of Basic Energy Sciences, Division of Materials Sciences and Engineering (contract no. DE-AC0276SF00515). C.L.B. acknowledges financial support from the Ramsay Memorial Fellowship Trust. Both M.K. and P.R.U. acknowledge support from Warwick-Monash Alliance Accelerator funding. Separately, P.R.U. acknowledges support from a Royal Society Wolfson Research Merit Award. Part of this work was performed at the Stanford Nano Shared Facilities (SNSF)/Stanford Nano-fabrication Facility (SNF), supported by the National Science Foundation under award ECCS-1542152. D.H.A. and N.J.S. acknowledge support from the DOE Office of Basic Energy Sciences SBIR program under awards DE-SC-0007691 and DE-SC-0009573. This research used resources of the Advanced Light Source, which is a DOE Office of Science User Facility under contract no. DE-AC02-05CH11231. We thank J. Lim, S. B. Kalirai, C. Baeumer, L. Zhang, Y.-L. Liang and C. E. D. Chidsey for discussions and assistance with the experiments.

Author contributions J.T.M. and W.C.C. developed the concept of the experiments, J.T.M. performed the synthesis, STXM, UV–vis, EQCM, RDE, SEM and XRD experiments. A.R.A. performed the EC-AFM and TEM experiments. P.R.U., M.K. and C.L.B. designed and performed the SECCM experiments. W.E.G. wrote the principal components analysis and non-negative matrix factorization code for the STXM data analysis. H.D.D. performed the EC-AFM image alignment. D.H.A. and N.J.S. designed and fabricated the STXM cell. Y.-S.Y. and D.A.S. assisted with the STXM experiments. All authors contributed to the discussion of the results and writing of the manuscript.

Competing interests D.H.A. and N.J.S. are employed by Hummingbird Scientific, which designed and manufactured the STXM microfluidic liquid cell used in these experiments.

Additional information
Supplementary information The online version contains supplementary material available at https://doi.org/10.1038/s41586-021-03454-x.
Correspondence and requests for materials should be addressed to J.T.M. or W.C.C.
Peer review information *Nature* thanks Shannon Boettcher, Marcel Risch and the other, anonymous, reviewer(s) for their contribution to the peer review of this work. Peer reviewer reports are available.
Reprints and permissions information is available at http://www.nature.com/reprints.